Scaling up Frequency-Comb-Based Optical Time Transfer to Long Terrestrial Distances

Jennifer L. Ellis,[1] Martha I. Bodine,[1,2] William C. Swann,[1] Sarah A. Stevenson,[1,2] Emily D. Caldwell,[2] Laura C. Sinclair,[1,*] Nathan R. Newbury,[1,†] and Jean-Daniel Deschênes[2,3,‡]

[1] *National Institute of Standards and Technology, Boulder, Colorado 80305, USA*
[2] *University of Colorado Boulder, Boulder, Colorado 80309, USA*
[3] *Octosig Consulting Inc., Quebec City, Quebec, Canada*

(Received 9 November 2020; revised 15 January 2021; accepted 21 January 2021; published 1 March 2021)

Frequency-comb-based optical two-way time and frequency transfer (O-TWTFT) can support future ultra-precise clock networks over free-space links. However, demonstrations have thus far only operated at one corner of a complex parameter space, which balances received optical power, timing performance, and update rate. Here, we analyze the performance of O-TWTFT across this parameter space, with a specific focus on extending the link distance at constant launch power and telescope aperture. We perform experiments across a three-node network spanning 28 km of turbulent air, and successfully demonstrate a more than 2000× reduction in the required received optical power corresponding to a potential 45× increase in distance. This distance increase does come with an associated reduction in timing precision, with the uncertainty increasing from 60 as to 20 fs at 10 s averaging times. However, this level of precision is still more than adequate for most applications. In addition, it comes with a reduction in sampling rate, which potentially limits this approach to static links. Interestingly, because this system optimization does not require any hardware modifications, O-TWTFT links could be dynamically tuned to support future long-distance optical clock networks over a range of conditions and applications.

DOI: 10.1103/PhysRevApplied.15.034002

I. INTRODUCTION

Frequency-comb-based optical two-way time and frequency transfer (O-TWTFT) transfers time and frequency information across open air paths to enable future networks of optical clocks [1]. To date, O-TWTFT has achieved femtosecond-level time transfer and 10^{-18} frequency transfer over city-scale free-space links [2–5]. However, one outstanding challenge for O-TWTFT is to increase its distance well beyond the current record of 14 km [5]. This increased distance could enable exciting applications of optical clock networks, including tests of general relativity [6], geodesy [7], very long baseline interferometry [8], dark matter searches [9,10], and the redefinition of the second [11,12].

O-TWTFT works through the exchange of frequency comb pulses between clock locations across a free-space link. In principle, the maximum operational distance can be extended by increasing either the launched optical power or the free-space telescope aperture to maintain enough signal-to-noise ratio (SNR) at the receiver. However, either approach is costly in power and system size. In addition, because O-TWTFT requires single-mode coherent detection, atmospheric turbulence limits the maximum useable aperture without invoking adaptive optics [13]. Instead, we show one can dramatically increase O-TWTFT's distance, at a fixed optical power and telescope aperture, by effectively slowing down the linear optical sampling upon which O-TWTFT relies to precisely measure the comb pulse arrival time to within femtoseconds. To do this, we increase the magnification factor, M, defined in the following, that characterizes the linear optical sampling. Here, we increase M by over 33 dB compared with previous work, leading to a corresponding 33 dB increase in SNR and a corresponding potential 45-fold increase in distance. This increase in link distance does come with tradeoffs in terms of a lower sampling rate and higher residual noise. We analyze these tradeoffs here through both theoretical analysis and experimental tests conducted over a 28-km free-space three-node network [5].

In O-TWTFT, as with other optical two-way time-frequency approaches [14–16], the reciprocity of bidirectional free-space links enables the removal of time-of-flight fluctuations to measure the time-frequency offset

*laura.sinclair@nist.gov
†nathan.newbury@nist.gov
‡octosigconsulting@gmail.com

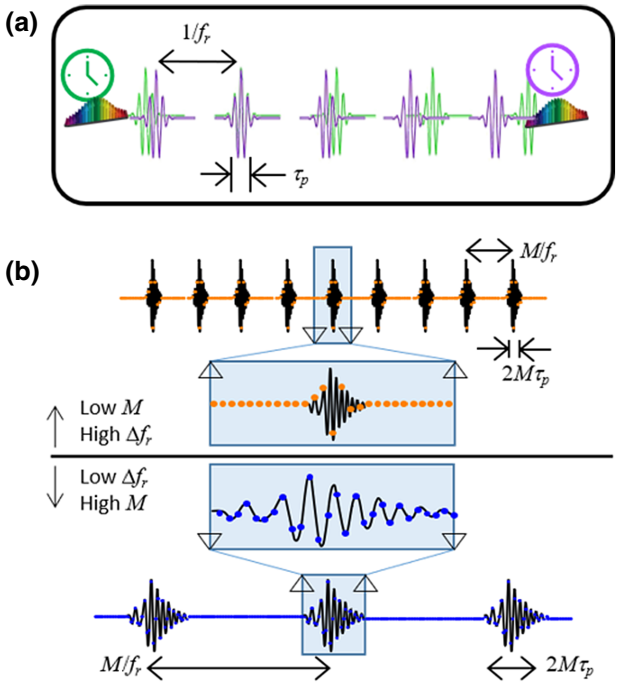

FIG. 1. (a) In comb-based O-TWTFT, the two end sites exchange frequency comb pulse trains with their repetition rates, f_r, offset by Δf_r. The comb pulses have femtosecond-level timing jitter and an intensity FWHM, τ_p, of a few hundred femtoseconds. (b) At each site, the heterodyne overlap between the two pulse trains leads to a series of interferograms that reflect the incoming comb pulses but magnified in time by a factor $M = f_r/\Delta f_r$. As indicated in the comparison between the upper and lower panels, a higher M means a greater number of pulses sample the interferogram (circles), yielding a correspondingly higher SNR after a matched filter.

between clocks [2–5,17,18]. Here, the clocks each consist of a frequency comb referenced to a cavity-stabilized laser. As indicated in Fig. 1, the relative clock timing is exchanged via the frequency-comb pulses across the link. O-TWTFT then uses linear optical sampling to determine the pulse arrival times with femtosecond precision [19,20], wherein the incoming frequency comb is set to a repetition frequency, f_r, that differs by a small known amount, Δf_r, from the local frequency comb. In this case, heterodyne detection of the incoming comb pulses with the local comb pulses yields a series of interferograms that repeat at a rate of Δf_r. These interferograms can be viewed as a sampled copy of the incoming pulse but with a time axis that is effectively magnified by a factor $M = f_r/\Delta f_r$. Therefore, the interferogram arrival times, or timestamps, are exactly the incoming comb pulse arrival times but magnified by M. A linear combination of the timestamps from each end of the link yields the relative time offset between the two end clocks A and B, Δt_{AB}, independent of the time-of-flight and at a sampling rate of $\Delta f_r = f_r/M$.

This whole process can only be accomplished if the interferogram SNR is high enough for detection. To optimize the SNR, we use matched-filter processing, a common signal processing technique of correlating the incoming signal with a template of the expected signal [21] (e.g., one previously measured with a shorted link), which removes chirp and coherently integrates the signal over the interferograms shown in Fig. 1(b). In the shot-noise limit, the resulting power SNR is the number of detected photons per interferogram, or

$$\mathrm{SNR} \approx 3\eta M \tau_P P_{\mathrm{rec}}/h\nu \tag{1}$$

where η is the quantum efficiency of the detector, $h\nu$ is the photon energy, τ_p is the intensity full-width half-maximum (FWHM) of the (unchirped) frequency comb pulses, and P_{rec} is the received optical power (see Appendix A). Given a minimum detectable SNR, inversion of Eq. (1) gives the corresponding minimum threshold received power, P_{min}, below which O-TWTFT fails. With strong turbulence, P_{rec} is not fixed but follows a gamma-gamma probability distribution function [22]. (See Appendix A.) In that case, we define the link availability, α, as the fraction of time the received power exceeds P_{min} and the mean sampling rate for the clock comparison becomes $\alpha\Delta f_r$.

From Eq. (1) and Fig. 1(b), the SNR increases with M simply because a greater number of comb pulses contribute to each interferogram. We can trade this increase in SNR for increased distance. Assuming the SNR falls quadratically with distance solely due to the increased diffraction of the transmitted comb light, every 100-fold increase in M results in a 10-fold increase in distance. (Note that this quadratic drop-off in SNR with distance represents the best-case scenario as increased atmospheric turbulence can further reduce the SNR with distance.) We are free to increase M until the interferogram centerburst duration reaches the turbulence-limited optical coherence time, t_{coh}, at which point decoherence limits the SNR. This argument yields $M_{\mathrm{max}} \sim t_{\mathrm{coh}}/(2\tau_p)$. For our system with the strong turbulence encountered here, we find $M_{\mathrm{max}} \sim 2 \times 10^8$ corresponding to $\Delta f_r \sim 1$ Hz at $f_r \sim 200$ MHz, which is 2000× larger than in Refs. [2–5].

This increase in M, and therefore system distance, is not without tradeoffs. As already mentioned, the sampling rate, $\alpha\Delta f_r$, is reduced (with consequences for moving platforms discussed below). In addition, the timing jitter will also increase. As derived in the Appendix B or following [2–5,17,18], the timing variance σ_t^2, in the O-TWTFT timing measurement on Δt_{AB}, for a fixed averaging time t_{avg} is

$$\sigma_t^2 \approx \frac{1}{\alpha\Delta f_r t_{\mathrm{avg}}}\left[\frac{\tau_p^2}{\mathrm{SNR}} + \delta t_c^2 + (2\pi M \Delta\beta_2 \delta f_c)^2\right] \tag{2}$$

where δt_c is the residual timing noise on the frequency combs and δf_c is their residual optical carrier frequency

noise. The prefactor is simply the inverse of the number of samples, reflecting the reduced sampling rate. Of the terms in brackets: the first term is the impact of shot noise on the uncertainty of timestamps, the second term is the residual timing noise from the combs, and the third term is the Gordon-Haus-like contribution [23]. This effect results from the presence of differential dispersion between the combs, $\Delta\beta_2$, which leads to dispersion on the measured interferogram. The matched filter removes this dispersion, outputting a pulse with a well-defined arrival time. However, if there is also relative optical carrier frequency noise, the matched-filter processing leads to an apparent timing shift that is proportional to the product of the differential dispersion and carrier frequency shift. Unfortunately, this Gordon-Haus-like contribution is amplified by the magnification factor because of the linear optical sampling [17,18,23]. Additional contribution to Eq. (2) from asynchronous sampling of atmospheric link delay variations [4,5] is eliminated here by tuning the relative transceivers delays so that the interferograms at opposite ends of the link are roughly simultaneous (see Appendix C). For our system, typical parameter values are $\tau_p = 282$ fs, $f_r = 200$ MHz, $\delta t_c = 5$ fs, $\Delta\beta_2 = 0.12$ ps^2, and $\delta f_c = 0.4$–30 kHz (see Appendix B). Equation (2) is for a single two-way link. Here, the system used the two links of an existing three-node network so this variance is doubled. For the case of white timing noise assumed here, this standard deviation, σ_t, is the same as the time deviation, and can be converted to the modified Allan deviation using the standard scaling laws [24,25].

II. EXPERIMENTAL DEMONSTRATION OF SCALING OF SNR AND TIMING WITH MAGNIFICATION FACTOR

To experimentally explore the tradeoffs inherent in (2), we use an existing three-node network spanning 28 km of turbulent air [5]. [A simple point-to-point network as in Fig. 1(a) would suffice but the three-node network was available.] We reference the two end clocks A and B to the same optical oscillator so that the expected clock offset, Δt_{AB}, is zero, making characterization of the O-TWTFT timing noise straightforward. To acquire timing data presented here, for values of $M > 10^6$, the centerburst of the interferogram is digitized at the full 200 MS/s sampling rate and the matched-filter processing occurs in real time within a field programmable gate array. For values of $M < 10^6$, data are continuously recorded at a reduced sampling rate of 2 MS/s with the matched-filter processing occurring as a postprocessing step. In both cases, computation of the clock offset and atmospheric link delay variations occur in postprocessing. We measure the performance as both links are attenuated by up to 50 dB while tuning Δf_r and thus M, over three orders of magnitude.

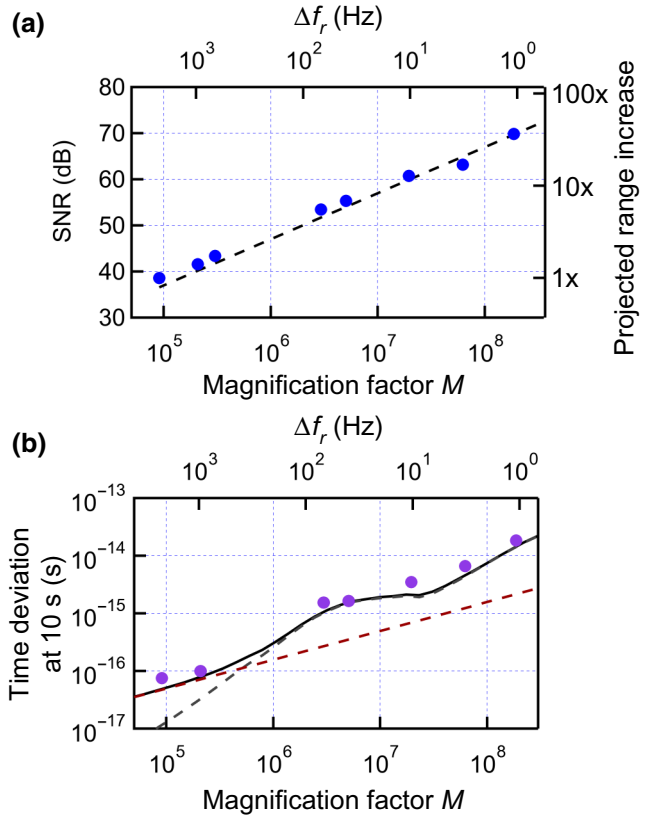

FIG. 2. (a) The measured interferogram SNR (circles) and calculated SNR (dashed line) versus magnification factor M (lower axis) or Δf_r (top axis) at a received power of ~12 nW (460 photons per comb pulse). The right axis gives the projected distance increase, assuming no other system modifications. (b) Measured time deviation at 10-second averaging time vs the magnification factor (lower axis) and Δf_r (upper axis) (filled circles) with the prediction from the residual comb timing noise (red dashed line), Gordon-Haus-like jitter (dashed) and total from Eq (2) (black line).

Figure 2(a) shows the measured interferogram SNR as a function of the magnification M. The excellent agreement with Eq. (1) over three orders of magnitude verifies the atmospheric optical coherence time exceeds the interferogram centerburst duration of $2M\tau_p = 120$ μs for $M = 2 \times 10^8$. A further five-fold increase in M (not shown) gives only a limited increase in SNR because the interferogram centerburst duration finally approaches t_{coh}. The right axis of Fig. 2(a) gives the corresponding projected distance increase, assuming a quadratic decrease in P_{rec} with distance, which is valid for smaller apertures or low enough turbulence.

We also characterize the corresponding measured timing noise, evaluated from the time deviation at $t_{avg} = 10$ s [Fig. 2(b)]. For these data, $P_{rec} \sim 12$ nW so $\alpha \sim 1$ and the SNR is high enough that the statistical contribution to Eq. (2) is negligible. The contribution from the comb timing jitter [second term in Eq. (2)] dominates

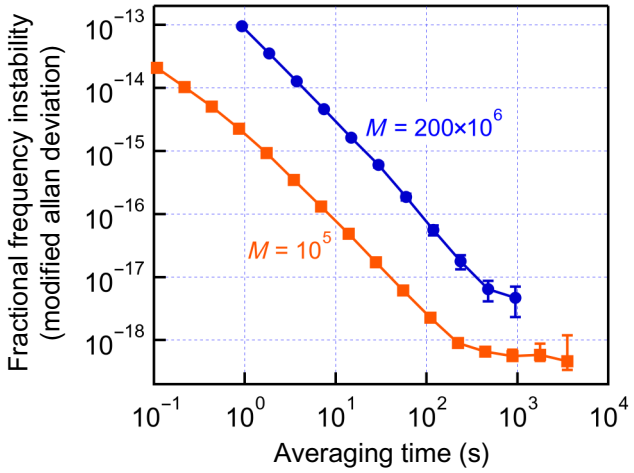

FIG. 3. Modified Allan deviation for $M = 200 \times 10^6$ ($\Delta f_r = 1$ Hz) and $M = 10^5$ ($\Delta f_r = 2.2$ kHz). To calculate these curves, we apply the corrections to the three-node data for asynchronous sampling at the node X site, as per Ref. [5].

for $M < 10^6$ ($\Delta f_r > 1$ kHz) [Fig. 2(b), red dashed line], but the Gordon-Haus-like jitter dominates at higher M ($\Delta f_r < 100$ Hz) [Fig. 2(b), gray line]. This contribution is not fundamental and could be reduced by minimization of both optical frequency noise and differential group-velocity dispersion $\Delta\beta_2$. Note that Eq. (2) assumes the timing variance decreases linearly with averaging time, which is only true for uncorrelated timing noise. For longer $t_{avg} \sim 100$–1000 s, O-TWTFT does reach a flicker noise floor. However, Fig. 3 verifies that the Allan deviations at longer times do reach a level of 10^{-18} even at the most extreme values of M.

III. OPERATION WITH INCREASED LINK LOSS AND MAGNIFICATION FACTOR

Next, we attenuate both bidirectional paths to increase the link loss, mimicking operation at longer distance. In Fig. 4, we consider the two extreme values of $M = 200 \times 10^6$ ($\Delta f_r = 1$ Hz) and $M = 9 \times 10^4$ ($\Delta f_r = 2.2$ kHz). When the full 4-mW power is launched, the median received power of 70 nW is well above P_{min} for both cases, and operation at $M = 9 \times 10^4$ gives both improved timing precision and a higher update rate of 2.2 kHz. However, if the link attenuation is increased by 50 dB, the median received power drops to only 700 fW, and operation at $M = 9 \times 10^4$ is prohibited whereas operation $M = 200 \times 10^6$ endures [Figs. 4(e) and 4(f)]. This series illustrates that modifying the system parameters can

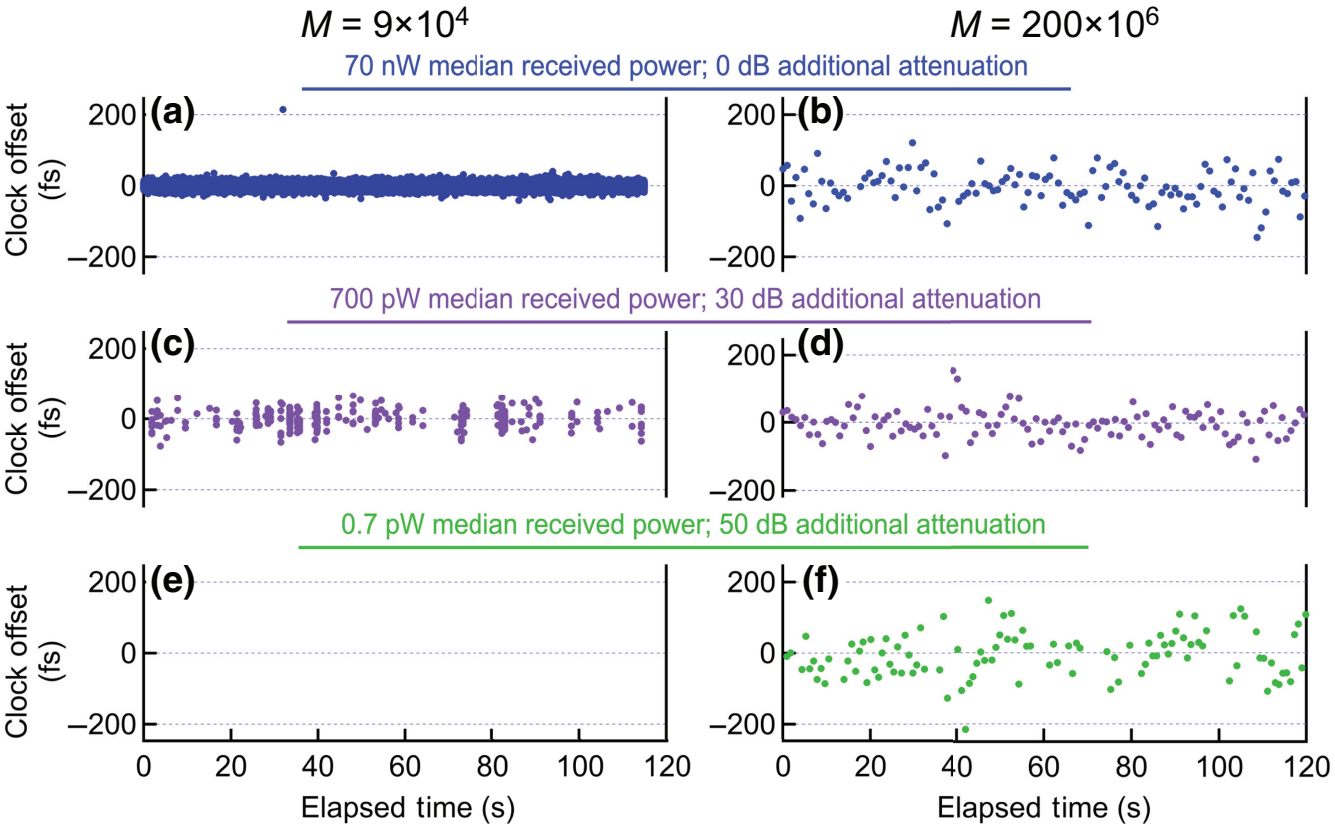

FIG. 4. The measured clock offset, Δt_{AB}, over the 28-km span of a three-node network at $M = 9 \times 10^4$ (left column) and $M = 200 \times 10^6$ (right column) at different median received powers.

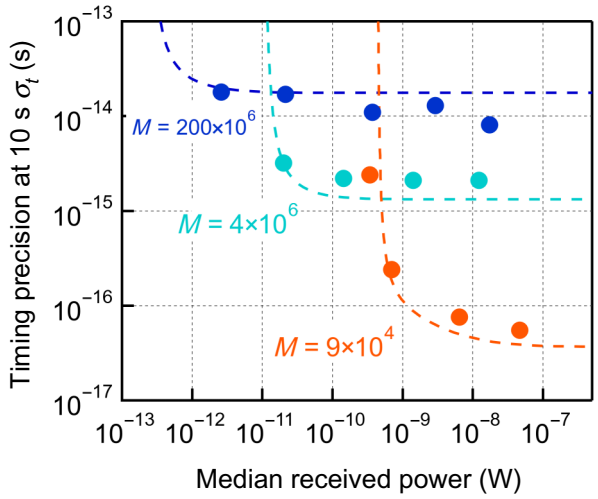

FIG. 5. Measured timing precision (time deviation), σ_t, vs the median received power at different M values (solid circles) and predicted performance from Eq. (2) (dashed lines). For a given M (Δf_r), the timing precision is roughly constant at high received power as it is dominated by comb timing noise and Gordon-Haus-like jitter. When the median received power drops close to P_{min}, the timing precision degrades significantly because of a dramatic increase in signal fades ($\alpha \to 0$) and increased statistical noise.

indeed enable time-frequency transfer when photons are scarce, albeit with reduced timing precision and update rate.

As a final illustration of these tradeoffs in O-TWTFT, we measure the timing precision (time deviation) at 10-s averaging as a function of received power for different values of M (Fig. 5). The agreement with Eq. (2) (dashed line) is very good considering the approximate parameter values and the three- to five-order-of-magnitude variation in both P_{rec} and M. In general, the performance is optimized by operating at the lowest possible M (highest Δf_r) for which the link availability, α, is at least 50%. Of course, this optimum depends on the integrated turbulence, which is a strong function of link length and of turbulence strength that will vary by orders of magnitude depending on the time-of-day or weather. To maintain optimum performance under such variable conditions, future O-TWTFT systems could be dynamically optimized by tuning the frequency combs to target an optimal M. Indeed, these data were acquired in just such a fashion by manually adjusting the locking conditions of the combs to achieve the desired M without making any other physical changes to the O-TWTFT system.

Here, the use of variable attenuation in the link serves as a proxy for an increased link distance. This argument is based on the fact that the three contributions to the short-term timing noise of Eq. (2) do not have any explicit dependence on link distance; the dependence on link distance is through the reduced SNR and link availability, α. As noted earlier, in the limit of diffractive loss, the SNR should decrease quadratically with link distance. An increase in link distance from 14 to 500 km, for example, then corresponds to 31 dB additional link loss, giving 500 pW received power in our case. From Fig. 5, at 500 pW, the timing precision at 10 s averaging should remain below 10 fs for $M > 4 \times 10^6$. If the path-integrated turbulence at such long link distances is high enough, the received power and SNR could drop by more than 31 dB, but this additional attenuation could be compensated for by further increasing M, subject to the previously discussed constraint of $M_{\text{max}} \sim t_{\text{coh}}/(2\tau_p)$. Equation (2) ignores two additional timing noise effects. First, Fig. 3 shows a flicker floor that is not included in Eq. (2). However, all evidence in this experiment and previous O-TWTFT has indicated this flicker floor is a result of transceiver noise and is independent of link distance. (This claim is based on the fact that the flicker floor is identical for a "shorted" link compared with the 14-km air path.) Second, as discussed in Appendix C, asynchronicity in the two-way sampling can lead to additional timing noise that is link-length dependent. Here, this effect is set close to zero by forcing synchronous sampling by adjusting the transceiver delays. However, for the 14-km link, the worst-case estimate of the excess timing noise due to asynchronous sampling is 6.5 fs for a 10-s averaging time, which occurs only at the largest value of $M = 200 \times 10^6$. Assuming the power spectral density (PSD) for the turbulence-induced time-of-flight noise scales linearly with link length, for a 500-km link we arrive at a worst-case estimate of 40 fs for the excess timing noise from asynchronous sampling. Of course, the ultimate test of O-TWTFT operation at such long distances will require experimental verification, but the scaling here suggests that long-distance terrestrial links should be feasible at the current 5-mW level launched comb powers.

Although O-TWTFT at high M is a promising approach to extend link distances for static links, there are further difficulties associated with moving platforms and future space-based links [26,27]. Previously, O-TWTFT has been demonstrated with motion up to 25 m/s at $M = 9 \times 10^4$ ($\Delta f_r = 2.2$ kHz) [17,18], but maintaining this performance at higher M (lower Δf_r) is problematic. First, the lower update rate limits the ability to track and remove the effects of platform motion. Second, there is an increased Gordon-Haus-like jitter associated with variable Doppler shifts. Third, Eq. (2) ignored the potential additional timing noise due to the apparent breakdown in reciprocity from asynchronous sampling (see Appendix C). Continuous suppression of this contribution for moving platforms at low sampling rates would require dynamic, adaptable transceiver delays. Taken together, these concerns may limit O-TWTFT with moving platforms to relatively high $M = 9 \times 10^4$, where the corresponding sampling rate of $\Delta f_r = 2.2$ kHz is sufficient to track changes in platform motion and limit the effects of asynchronous sampling.

IV. CONCLUSION

We have explored the balance between interferogram magnification factor and timing performance in O-TWTFT. We have demonstrated a significant increase in the SNR of over 33 dB and a corresponding potential 45× increase in distance is possible with no changes in hardware or system design, simply by adjusting the comb locking parameters. With such adjustments and based on the SNR-scaling demonstrated here, the current 14-km distance could be optimistically scaled up to as much as ∼500 km, which is well beyond any reasonably achievable terrestrial link distance. Alternatively, this improved SNR could be leveraged to enable the use of much smaller telescope apertures or lower launch powers for significantly reduced system size, weight, and power (SWaP). This improved SNR does come with a reduction in the timing precision from 60 as to up to 20 fs at 10-s averaging time. However, even at a degraded 20-fs precision and a 1-s update rate, the O-TWTFT performance is more than sufficient for linking high-performance optical clocks, and operation of O-TWTFT at high M (or very low Δf_r) should be able to support long-distance, low-power free-space time-frequency transfer.

ACKNOWLEDGMENTS

We thank Brian Washburn and Fabrizio Giorgetta for helpful comments on the manuscript. We acknowledge funding from the Defense Advanced Research Projects Agency Defense Sciences Office and the National Institute of Standards and Technology.

APPENDIX A: DERIVATION OF THE SNR [Eq. (1)]

We assume a Gaussian pulse, although a different pulse shape would result in only small changes in the numerical factors. We use the same notation as in the main text. The derivation of SNR in Eq. (1) of the main text closely follows Chapter 2 in Ref. [28] as well as previous discussions of O-TWTFT [2,18].

We consider a "signal" and "local oscillator" (LO) frequency comb at repetition rates $f_r = T_r^{-1}$ and $f_r + \Delta f_r = (T'_r)^{-1}$. Their power, averaged over a few optical cycles, is

$$\begin{aligned} P_s(t) &= n_s h\nu \sum_k \left(\frac{1}{\sigma_P\sqrt{2\pi}}\right) e^{-(t-t_0-kT_r)^2/2\sigma_p^2} \\ P_{\mathrm{LO}}(t) &= n_{\mathrm{LO}} h\nu \sum_m \left(\frac{1}{\sigma_P\sqrt{2\pi}}\right) e^{-(t-mT'_r)^2/2\sigma_p^2} \end{aligned} \tag{A1}$$

where n_s is the number of signal photons per pulse, n_{LO} is the number of LO photons per pulse, the Gaussian width, σ_p, is related to the intensity FWHM as $\tau_p = 2\sqrt{2\ln(2)}\sigma_p$, t_0 is the slowly varying relative time offset of the signal comb compared with the LO comb, and the integer k or m label the pulse number. In the limit of no chirp, the electric field of each pulse is just the square root of each term in (A1) with an additional carrier frequency. As in Refs. [2,18], the interferogram is the correlation of these electric fields, after a low pass filter, which is

$$s(t) = 2\eta\sqrt{n_s n_{\mathrm{LO}}} e^{-(t-Mt_0)^2/8M^2\sigma_p^2} \cos(2\pi f t + \theta) \tag{A2}$$

where $M = f_r/\Delta f_r$ is the magnification, f is the offset in carrier frequency between the two pulse trains, θ is their phase offset, and η is the detection quantum efficiency. Note that this interferogram has a FWHM of $2M\tau_p$, where one factor of $\sqrt{2}$ arises from the electric field pulse width compared with the intensity pulse width, one factor of $\sqrt{2}$ arises from the cross-correlation. The magnification of the linear optical sampling approach is evident in the exponent of the Gaussian; a small change in the signal pulse arrival time, t_0, results in an M times larger change in the interferogram arrival time. Finally, note that Eq. (A2) reduces to the usual expression for coherent heterodyne detection between continuous-wave lasers [28] at the center of the interferogram, $t = Mt_0$, or in the limit $\sigma_p \to \infty$.

The measured interferogram is the previous expression plus additional shot noise, written as

$$r(t) = s(t) + w \tag{A3}$$

where w is a zero-mean, white random process with variance $\langle w^2 \rangle = \eta n_{\mathrm{LO}}$, and a corresponding single-sided noise power $N_0 = 2f_r^{-1}\eta n_{\mathrm{LO}}$. In general, there can be differential spectral chirp between the pulses, which is not included in Eq. (A2). To remove this chirp and to maximize the SNR, we apply a matched filter to this signal of $Cs(-t)$, where the normalization C is chosen to preserve the peak signal.

The result is the matched-filtered interferogram

$$r_{\mathrm{MF}}(t) = 2\eta\sqrt{n_s n_{\mathrm{LO}}} e^{-(t-Mt_0)^2/16M^2\sigma_p^2} \cos(2\pi f t) + w_{\mathrm{MF}} \tag{A4}$$

which has a $\sqrt{2}$-broader FWHM of $2\sqrt{2}M\tau_p$ than the unfiltered interferogram envelope and a filtered white noise, w_{MF}, with reduced variance. Rather than calculate the variance of this filtered white noise, we can directly find the power SNR by way of the matched-filter theorem, which states that the SNR is given by

$$\begin{aligned} \mathrm{SNR} &= \frac{\int s^2(t)dt}{N_0/2} \\ \mathrm{SNR} &= 4\sqrt{\pi} f_r \eta n_s M \sigma_p \\ \mathrm{SNR} &\approx \frac{3\eta M \tau_p P_{\mathrm{rec}}}{h\nu} \end{aligned} \tag{A5}$$

where the received signal power is $P_{\mathrm{rec}} \equiv n_s h\nu f_r$, we assume $f \gg \sigma_p^{-1}$ (corresponding to heterodyne rather than homodyne detection), and we rewrote the equation in

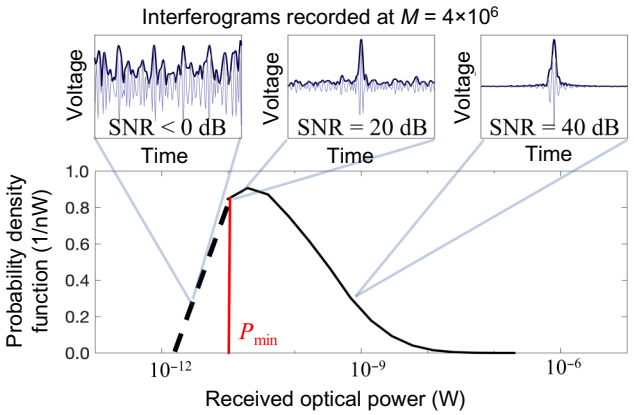

FIG. 6. Example probability distribution function of the received power after 10 dB additional attenuation. Above the minimum received power, $P_{\min}$ [red line, shown for $M = 4 \times 10^6$ ($\Delta f_r = 50$ Hz)], there is sufficient SNR to measure a timestamp, but below $P_{\min}$ the SNR of the interferograms is too low. Inset: Measured interferograms (gray line) and their envelope (black line) at different received powers and SNRs.

terms of the intensity FWHM of the comb pulse, $\tau_p = 2\sqrt{2\ln(2)}\sigma_p$. This is exactly Eq. (1) in the main text. Again, this derivation assumed zero differential chirp between the comb pulses, which is not the case. However, because the matched-filter removes any chirp, both Eqs. (A4) and (A5) are unchanged in the presence of differential chirp.

Finally, a shorter heuristic derivation yields the same result. In the shot-noise limit, the power SNR for the interferogram should simply be the number of detected signal photons. This number is given by $n_s \times \left(2\sqrt{2}M\tau_p f_r\right)$, where the term in parenthesis is the number of signal photon pulses that occur during the FWHM duration of the centerburst of the matched-filter interferogram from Eq. (A4). In so much as $2\sqrt{2} \approx 3$, we again arrive at Eq. (A5).

As noted in the main text, the received power varies because of turbulence. Figure 6 gives an example measured histogram of received power and shows the corresponding interferograms at different SNR for one value of M.

APPENDIX B: DERIVATION OF THE TIMING VARIANCE [Eq. (2)]

Consider a link between two end sites, labeled A and B. At each site, we find the peak of the matched-filtered interferograms, Eq. (A4), to extract their center location, Mt_0 . To generate timestamps at each site, we then divide this quantity by the known magnification factor, M, and relabel $t_0 \to t_{\mathrm{BA}}$ at site A and $t_0 \to t_{\mathrm{AB}}$ at site B. These two timestamps, t_{AB} and t_{BA}, will vary both because of time offsets between the A and B clocks, denoted Δt_{AB}, and because of time-of-flight variations. As per two-way time transfer, we remove the common time-of-flight variations by taking a linear combination of timestamps to find $\Delta t_{\mathrm{AB}} = (t_{\mathrm{AB}} - t_{\mathrm{BA}})/2$.

Any uncertainty in the extracted values of the timestamps will lead to residual noise on the measurement of Δt_{AB}. Let us assume the two combs are identical, for simplicity. If the variance in the measured timestamp for either end site is δt_0^2, the resulting variance in the measured clock offset, Δt_{AB}, is

$$\sigma_t^2 = \frac{1}{2}\delta t_0^2 \tag{B1}$$

If we assume that the noise in the measured t_0 is uncorrelated between interferograms, i.e., the uncertainty is dominated by white phase/timing noise (which is a reasonable assumption at short times), then this variance averages down linearly with the number of measurements, and we can write

$$\sigma_t^2 = \frac{1}{\alpha \Delta f_r t_{\mathrm{avg}}}\left[\delta t_c^2 + \delta t_{\mathrm{statistical}}^2 + \delta t_{\mathrm{GHjitter}}^2\right] \tag{B2}$$

where $(\alpha \Delta f_r t_{\mathrm{avg}})$ is the number of interferograms within the averaging time, t_{avg}, including the link availability, α, and we have rewritten the variance in the timestamps as $\delta t_0^2 \equiv 2[\delta t_c^2 + \delta t_{\mathrm{statistical}}^2 + \delta t_{\mathrm{GHjitter}}^2]$, to delineate the contribution from comb timing noise, statistics, and carrier frequency noise, respectively. Next, we evaluate each of these distinct contributions.

First, there will be residual timing noise on each frequency comb pulse train with variance δt_c^2 because of imperfect phase locks to the local optical oscillator, for example. The corresponding contribution to the variance of the timestamps is double, because two combs contribute, but this is then halved by Eq. (B1), leading to the term in Eq. (B2). Based on the measured timing noise of the phase-locks for the fiber frequency combs with additional contribution from the short out-of-loop fiber paths, we measure $\delta t_c^2 \approx (5\text{ fs})^2$ (see Refs. [2–5,14,15]).

Second, there will be a statistical contribution to the extracted interferogram timing owing to its limited SNR. The resulting variance is $\delta t_0^2 \approx 2\tau_p^2/\mathrm{SNR}$for a Gaussian, where the numerical prefactor is most easily derived numerically. From Eq. (B1), this leads to a contribution

$$\delta t_{\mathrm{statistical}}^2 = \frac{\tau_p^2}{\mathrm{SNR}}. \tag{B3}$$

For our system, the FWHM of the unchirped comb pulse is $\tau_p \approx 280$ fs, as measured either by Fourier transforming the pulse intensity spectrum or, equivalently, from the measured FWHM of the matched-filter interferogram.

Third, there is a contribution from Gordon-Haus-like timing jitter on the measured matched-filter interferograms. This effect arises only if there is residual differential

spectral chirp between the two comb pulses, caused for example by the fact the two comb pulses might have travelled down different lengths of fiber optic before being interfered for heterodyne detection. With dispersion, any differential carrier frequency noise is converted to differential timing noise. In this case, the situation is exacerbated because this timing noise is amplified by the magnification factor, as was derived in Refs. [17,18]. Following Eq. (A5) of Ref. [18] (after correcting for a factor of two error) and using Eq. (B1), we have the contribution

$$\delta t^2_{\mathrm{GHjitter}} = 4\pi^2 \Delta\beta_2^2 M^2 \delta f_c{}^2 \tag{B4}$$

where $\Delta\beta_2$ is the differential dispersion between the signal and LO comb pulses, and $\delta f_c{}^2$ is the carrier frequency noise on a single comb. For our system, we measure the differential dispersion directly from the spectral phase of the Fourier-transformed interferogram to be $\Delta\beta_2 \approx 0.12$ ps^2, which arises from the relative quadratic phase between the two combs.

Optical frequency noise, $\delta f_c{}^2$, within the three-node network comes from two sources. First, there are residuals on the phase lock of the frequency combs to their reference oscillators (i.e., cavity-stabilized lasers). Second, there is relative frequency drift between the reference oscillator of the intermediate Node X compared with the common reference oscillator for Nodes A and B. (This second noise source is specific to the three-node configuration used here.) Figure 7 shows the frequency noise PSD from these two contributions. We estimate $\delta f_c{}^2$ by integrating the total PSD in Fig. 7 up to Fourier frequencies of $\left(2\sqrt{2}M\tau_p\right)^{-1}$, or the inverse of the effective matched-filter interferogram centerburst duration. Fluctuations on faster timescales are averaged across the interferogram. The value is insensitive to the lower limit, chosen here to be 1 Hz for simplicity. The carrier frequency distances from $\delta f_c{}^2 \approx (0.37\ \mathrm{kHz})^2$ at $M = 200 \times 10^6$ ($\Delta f_r = 1$ Hz) to $\delta f_c{}^2 \approx (32\ \mathrm{kHz})^2$ at $M = 9 \times 10^4$ ($\Delta f_r = 2.2$ kHz). As shown in Fig. 2 of the main text, this Gordon-Haus-like jitter dominated the residual timing noise. However, it is not a fundamental limitation and future systems could minimize this effect by decreasing both the optical frequency noise and the differential dispersion.

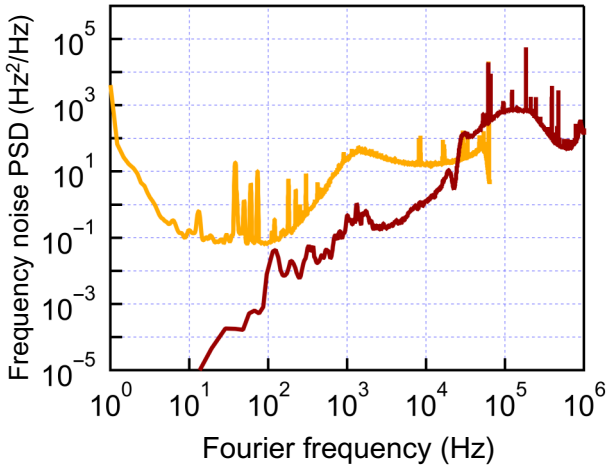

FIG. 7. PSD of optical frequency noise. There are two sources of optical frequency noise for this the three-node network. First, the residuals of the frequency comb's optical locks (red). Second, the relative cavity drift between the reference oscillator for sites A and B vs the reference oscillator for site X (light orange). The total frequency noise PSD is the sum of these two PSDs. For the purpose of calculating the total frequency noise variance, this measured PSD is extended to higher Fourier frequency assuming white frequency noise beyond 1 MHz.

Insertion of Eqs. (B3) and (B4) into Eq. (B2) yields

$$\sigma_t^2 \approx \frac{1}{\alpha \Delta f_r t_{\mathrm{avg}}}\left[\frac{\tau_p^2}{\mathrm{SNR}} + \delta t_c^2 + (2\pi M \Delta\beta_2 \delta f_c)^2\right] \tag{B5}$$

or Eq. (2) in the main text. As noted earlier, this equation assumes uncorrelated timing noise between interferograms and is only valid then for shorter averaging times where uncorrelated "fast" noise dominates. It ignores the flicker floor. As shown in Fig. 3, this is a valid assumption for averaging times up to many tens of seconds. In addition, we have ignored the fact that both the prefactor and statistical contribution are power dependent so that, technically, they should both be averaged over the received power distribution.

APPENDIX C: TIMING JITTER FROM ASYNCHRONOUS SAMPLING

The derivation given previously ignores the additional timing noise associated with asynchronous sampling across the two-way link [4,5]. If the interferograms at each end of the link are not measured simultaneously, the optical pulses contributing to the two interferograms measured on either side of the link traverse the free-space link at different times. As a result, the sampled atmospheric path length variations will no longer perfectly cancel in the two-way sum and this will contribute to timing uncertainty. This asynchronous sampling time offset, δt_a, at the two ends of the link can vary from 0 s to $(2\Delta f_r)^{-1}$. A related timing noise is caused by fluctuations in the clock offset itself, where asynchronous sampling again produces timing errors, but this contribution will be ignored as the treatment is the same and is expected to be smaller than the atmospheric contribution.

This effect manifests in different ways depending on the timescales associated with path length variations compared with the sampling rate (Δf_r). When these fluctuations are slow compared with the sampling rate, they can be corrected for if we have calibrated the system to determine

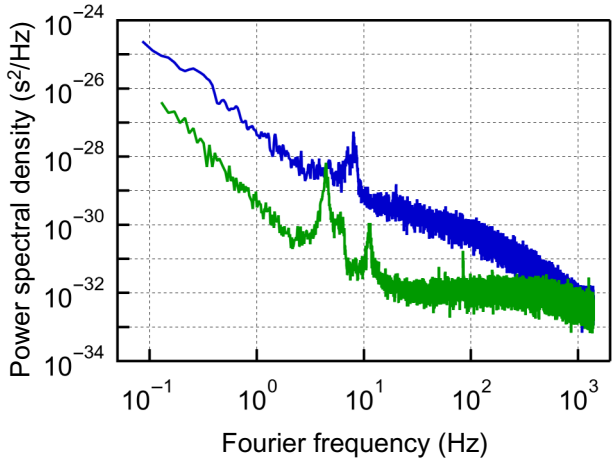

FIG. 8. Measured PSD for the time-of-flight, S_T, across the 14-km link (blue curve). (This quantity is measured by taking the opposite linear combination of timestamps to that used for the clock comparison). For comparison, we also show the PSD of the relative clock noise (green curve) between the two sites, which is lower in this case.

δt_a [5]. However, if either the clock offset or time-of-flight vary rapidly compared with the sampling rate, aliasing results and correction is not possible so that there is an increased timing noise on the clock offset measurement. As an estimate of this effect, the additional timing noise from aliased time-of-flight fluctuations will be

$$\delta t^2_{\text{asynch}} \approx \int_{\delta t_a^{-1}}^{\infty} S_T(\nu) d\nu \tag{C1}$$

where $S_T(\nu)$ is the PSD for time-of-flight variations as a function of Fourier frequency ν (see Fig. 8). A similar expression applies for the contribution from the clock variations. This effect depends on Δf_r because, as noted previously, δt_a must fall between 0 s and $1/2\Delta f_r$ s. As we increase M, Δf_r decreases and δt_a can take on very large values. At our minimum $\Delta f_r = 1$ Hz, the lower limit to the integration can approach 0.5 Hz, leading to significant timing noise on the order of $\delta t^2_{\text{asynch}} \approx (20\text{ fs})^2$ for our 14-km turbulent link (from the PSD in Fig. 8) for a single measurement. As these are uncorrelated from measurement to measurement, the corresponding timing noise at 10-s averaging would be $\delta t_{\text{asynch}}(10\text{ s}) \approx 6.5$ fs. To avoid this effect here, we have adjusted the delays in the transceiver to make sure the sampling is synchronous, i.e., δt_a to $\sim$1 ms even at $\Delta f_r = 1$ Hz. However, in many implementations this nulling of the asynchronous time offset may not be practical or even possible, for example if there is significant platform motion. Consequently, asynchronous sampling may provide limitations for future links between moving platforms operating at low magnification or Δf_r.

[1] F. Riehle, Optical clock networks, Nat. Photonics **11**, 25 (2017).

[2] J.-D. Deschênes, L. C. Sinclair, F. R. Giorgetta, W. C. Swann, E. Baumann, H. Bergeron, M. Cermak, I. Coddington, and N. R. Newbury, Synchronization of Distant Optical Clocks at the Femtosecond Level, Phys. Rev. X **6**, 021016 (2016).

[3] L. C. Sinclair, W. C. Swann, H. Bergeron, E. Baumann, M. Cermak, I. Coddington, J.-D. Deschênes, F. R. Giorgetta, J. C. Juarez, I. Khader, K. G. Petrillo, K. T. Souza, M. L. Dennis, and N. R. Newbury, Synchronization of clocks through 12 Km of strongly turbulent air over a city, Appl. Phys. Lett. **109**, 151104 (2016).

[4] L. C. Sinclair, H. Bergeron, W. C. Swann, E. Baumann, J.-D. Deschênes, and N. R. Newbury, Comparing Optical Oscillators Across the air to Milliradians in Phase and 10–17 in Frequency, Phys. Rev. Lett. **120**, 050801 (2018).

[5] M. I. Bodine, J. L. Ellis, W. C. Swann, S. A. Stevenson, J.-D. Deschênes, E. D. Hannah, P. Manurkar, N. R. Newbury, and L. C. Sinclair, Optical time-frequency transfer across a free-space, three-node network, APL Photonics **5**, 076113 (2020).

[6] P. Delva, A. Hees, and P. Wolf, Clocks in space for tests of fundamental physics, Space Sci. Rev. **212**, 1385 (2017).

[7] T. E. Mehlstäubler, G. Grosche, C. Lisdat, P. O. Schmidt, and H. Denker, Atomic clocks for geodesy, Rep. Prog. Phys. **81**, 064401 (2018).

[8] C. Clivati, R. Ambrosini, T. Artz, A. Bertarini, C. Bortolotti, M. Frittelli, F. Levi, A. Mura, G. Maccaferri, M. Nanni, M. Negusini, F. Perini, M. Roma, M. Stagni, M. Zucco, and D. Calonico, A VLBI experiment using a remote atomic clock via a coherent fibre link, Sci. Rep. **7**, 40992 (2017).

[9] A. Derevianko and M. Pospelov, Hunting for topological dark matter with atomic clocks, Nat. Phys. **10**, 933 (2014).

[10] Y. V. Stadnik and V. V. Flambaum, Searching for Dark Matter and Variation of Fundamental Constants with Laser and Maser Interferometry, Phys. Rev. Lett. **114**, 161301 (2015).

[11] S. Bize, The unit of time: Present and future directions, Comptes Rendus Phys. **20**, 153 (2019).

[12] F. Riehle, Towards a redefinition of the second based on optical atomic clocks, Comptes Rendus Phys. **16**, 506 (2015).

[13] D. L. Fried, Optical heterodyne detection of an atmospherically distorted signal wave front, Proc. IEEE **55**, 57 (1967).

[14] K. Djerroud, O. Acef, A. Clairon, P. Lemonde, C. N. Man, E. Samain, and P. Wolf, Coherent optical link through the turbulent atmosphere, Opt. Lett. **35**, 1479 (2010).

[15] B. P. Dix-Matthews, S. W. Schediwy, D. R. Gozzard, E. Savalle, F.-X. Esnault, T. Lévèque, C. Gravestock, D. D'Mello, S. Karpathakis, M. Tobar, and P. Wolf, Point-to-Point stabilised optical frequency transfer with active optics, Nat. Commun. **12**, 515 (2021).

[16] H. J. Kang, J. Yang, B. J. Chun, H. Jang, B. S. Kim, Y.-J. Kim, and S.-W. Kim, Free-Space transfer of comb-rooted optical frequencies over an 18 km open-air link, Nat. Commun. **10**, 1 (2019).

[17] H. Bergeron, L. C. Sinclair, W. C. Swann, I. Khader, K. C. Cossel, M. Cermak, J.-D. Deschênes, and N. R. Newbury, Femtosecond time synchronization of optical clocks off of a flying quadcopter, Nat. Commun. **10**, 1819 (2019).

[18] L. C. Sinclair, H. Bergeron, W. C. Swann, I. Khader, K. C. Cossel, M. Cermak, N. R. Newbury, and J.-D. Deschênes, Femtosecond optical two-way time-frequency transfer in the presence of motion, Phys. Rev. A **99**, 023844 (2019).

[19] C. Dorrer, D. C. Kilper, H. R. Stuart, G. Raybon, and M. G. Raymer, Linear optical sampling, IEEE Photonic Technol. Lett. **15**, 1746 (2003).

[20] I. Coddington, W. C. Swann, and N. R. Newbury, Coherent linear optical sampling at 15 bits of resolution, Opt. Lett. **34**, 2153 (2009).

[21] M. A. Richards, *Fundamentals of Radar Signal Processing*, 2nd ed. (McGraw-Hill Education, New York, NY, USA, 2014).

[22] L. C. Andrews and R. L. Phillips, *Laser Beam Propagation Through Random Media*, 2nd ed. (SPIE, Bellingham, WA, 2005).

[23] J. P. Gordon and H. A. Haus, Random walk of coherently amplified solitons in optical fiber transmission, Opt. Lett. **11**, 665 (1986).

[24] IEEE Standard Definitions of Physical Quantities for Fundamental Frequency and Time Metrology - Random Instabilities, IEEE Std 1139-1999 1 (1999).

[25] W. Riley and D. A. Howe, *Handbook of Frequency Stability Analysis* (U.S. Government Printing Office, Washington, DC, 2008).

[26] C. Robert, J.-M. Conan, and P. Wolf, Impact of turbulence on high-precision ground-satellite frequency transfer with two-way coherent optical links, Phys. Rev. A **93**, 033860 (2016).

[27] A. Belmonte, M. T. Taylor, L. Hollberg, and J. M. Kahn, Effect of atmospheric anisoplanatism on earth-to-satellite time transfer over laser communication links, Opt. Express **25**, 15676 (2017).

[28] R. H. Kingston, *Detection of Optical and Infrared Radiation* (Springer, New York, 1978).